Real-time imaging and tracking of ultrastable organic dye nanoparticles in living cells

Accepted Manuscript

Real-time imaging and tracking of ultrastable organic dye nanoparticles in living cells

Ruirui Xu, Liming Huang, Weijia Wei, Xianfeng Chen, Xiaohong Zhang, Xiujuan Zhang

PII: S0142-9612(16)30084-9

DOI: 10.1016/j.biomaterials.2016.03.045

Reference: JBMT 17435

To appear in: *Biomaterials*

Received Date: 16 December 2015

Revised Date: 23 March 2016

Accepted Date: 30 March 2016

Please cite this article as: Xu R, Huang L, Wei W, Chen X, Zhang X, Zhang X, Real-time imaging and tracking of ultrastable organic dye nanoparticles in living cells, *Biomaterials* (2016), doi: 10.1016/j.biomaterials.2016.03.045.

Real-time imaging and tracking of ultrastable organic dye nanoparticles in living cells

Ruirui Xu[a], Liming Huang[a], Weijia Wei[a], Xianfeng Chen[b,*], Xiaohong Zhang[a], and Xiujuan Zhang[a,*]

[a]*Institute of Functional Nano & Soft Materials (FUNSOM), Jiangsu Key Laboratory for Carbon-Based Functional Materials & Devices, Soochow University, Suzhou Jiangsu 215123, P. R. China.*

[b]*School of Chemistry and Forensic Sciences, Faculty of Life Sciences, University of Bradford, United Kingdom, BD7 1DP.*

*Correspondence should be sent to E-mails: xjzhang@suda.edu.cn, xianfeng_chen@hotmail.com

Abstract*:*

Semiconductor quantum dots and upconversion nanoparticles have been broadly used for live cell imaging due to their color tunability and photostability etc. However, these inorganic materials often contain heavy metals and potentially have metabolism problems. To overcome these issues, herein, we report a type of organic dye nanoparticles (NPs) with coating of a thin silica layer and folic acid targeting molecules on the surface for live cell imaging. These organic NPs possess superior characteristics of high fluorescence intensity, large Stokes shift, good photostability, emission in the NIR range, and targeted delivery, enabling them to be a powerful fluorescent probe for living cell imaging. In our study, we successfully demonstrate their applications in investigating cell division, exploring the cellular uptake kinetics and pathway of NPs, observing the distribution of NPs, and live-time tracking the trajectory of specific NPs. Considering the excellent properties and unique clathrin- and caveollae-independent intracellular uptake pathway, we expect that this type of organic dye NPs will play an important role in live cell imaging.

Keywords: Organic fluorescence probes; Organic nanoparticles; Near-infrared emission; Live-time tracking; Live cell imaging

1. Introduction

Live cell imaging is an ideal way for continuous observation of the activities within living cells and becomes increasingly important for cell biology and cancer biology as well as many biomedical related applications [1,2]. It has now become a routine tool in biomedical and life science research, and is key to understanding organismal development by monitoring interactions within and among cells during their growth and differentiation. Live cell imaging techniques play a significant role in biological studies and biomedical engineering. It is increasingly important to apply these technologies to gain critical insight of biological activities in sub-cellular and molecular levels in living cells [3,4]. For this, various luminescent materials have been explored [5-8]. Compared with conventional fluorescence dyes for imaging, semiconductor quantum dots are highly photostable and bright [9-11]. Also attractively, their emission spectra can be conveniently tuned across a wide wavelength range by changing the composition and size. This unique characteristic makes quantum dots particularly suitable for multicolor detection. Except semiconductor quantum dots, lanthanide ion doped upconvertion nanoparticles (UCNPs) which possess good photostability and non-invasion of NIR excitation have also been successfully used for real-time imaging and tracking in living cells [12,13]. Although these materials are effectively applied for live cell imaging, these probes are composed of inorganic materials such that the metabolism of heavy metals must be taken into consideration. Particularly, many semiconductor quantum dots possess high toxicity and this seriously limits their practical applicability [14,15].

To avoid the safety issue, it is intriguing to adopt organic materials in live cell

imaging. In comparison with inorganic imaging materials, organic molecules can be more biocompatible and provide much wider choices in variety [16,17]. However, the application of isolated organic fluorophores has been hindered by their poor photostability for a long period of time [18], until organic dye NPs with the characteristic of aggregation-induced mission (AIE) were discovered in recent years [19,20]. AIE organic dyes are weakly fluorescent or even do not possess fluorescence in solution but become highly emissive when aggregated into NPs. These NPs can achieve enhanced fluorescence emission with remarkable photostability and excellent biocompatibility. Therefore, this material holds a bright future for practical applications in live cell imaging. In this study, we fabricated a novel type of AIE NPs with an ultra-thin layer of silica coating on the surface and used it for live cell imaging (Scheme 1). These NPs possess large absorptivity, intense emission in NIR region, large Stokes shift, excellent biocompatibility, strong photobleaching resistance, and specific cell targeting ability, which renders them suitable for imaging with high sensitivity of detection. Beyond the superior properties of fluorescent probe materials, when they are used in living organisms, it is also essential to understand the interaction between the materials and cells [21,22]. Therefore, we systematically investigated the cellular uptake mechanism of the NPs and observed the distribution and intracellular transport as well as the cells' behavior during their interaction with the nanostructure. The unique characteristic of our AIE NPs is that they enter cell through clathrin- and caveolae-independent endocytosis and this can lead to many advantages.

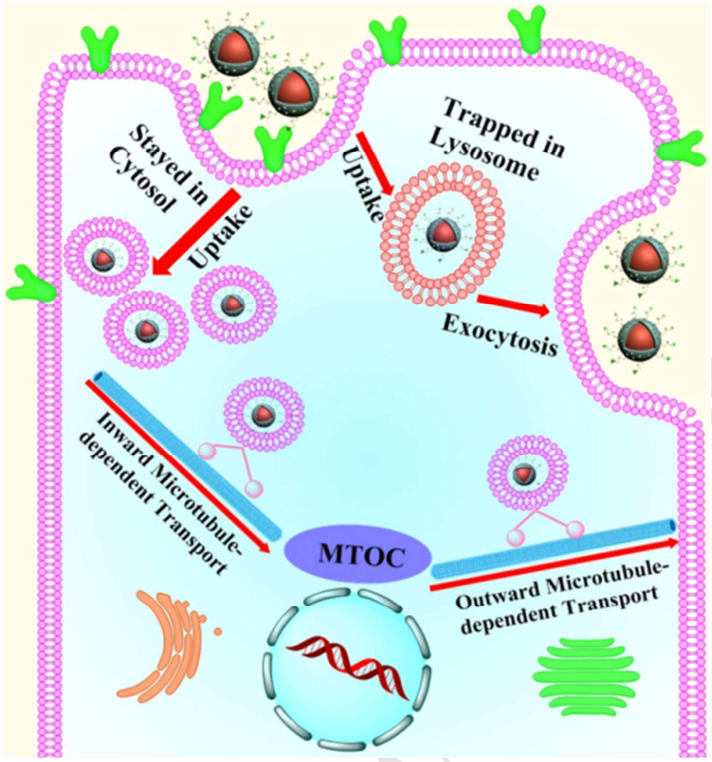

Scheme 1. Illustrations for the interaction between nanoparticles and cellular components.

2. Experimental section

2.1. Materials

N-phenyl-substitutedamine, tetramethylorthosilicate (TMOS), 4-bromophenylacetonitrile, N-hydroxysuccinimide (NHS), $P(t\text{-}Bu)_3$, 1-ethyl-3-(3-dimethylaminopropyl)-carbodiimidehydrochloride (EDC), $Pd(OAc)_2$, 2,7-di(4-(diphenylamino)phenyl-2,1,3-benzothiadiazol-7-yl) -9,9'-spirobifluorene (Spiro-BTA), hexadecyltrimethylammonium bromide (CTAB), 3-Aminopropyltriethoxysilane (APTES), folic acid (FA), chlorpromazine hydrochloride, cytisine, amiloride hydrochloridedehydrate, nocodazole and cytochalasin D were from J&K Scientific Ltd. Chloroform, triethylamine, methanol,

toluene, dichloromethane, petroleum, diethyl ether, and iodine were ordered from Sinopharm Chemical Reagent Co Ltd. Roswell Park Memorial Institute-1640 (RPMI-1640) medium, FA-free RPMI-1640, fetal bovine serum (FBS), 4',6-diamidino-2-phenylindole (DAPI), LysoTracker Green DND-26, and penicillin-streptomycin solution were obtained from Invitrogen (SanDiego, CA).

3-(4,5-dimethylthiazol-2-yl)-2,5-diphenyltetrazolium bromide (MTT) was ordered from Sigma Aldrich (Milwaukee, WI). A human nasopharyngeal epidermal carcinoma cell line (KB cell) and HL-7702 cell were received from American Type Culture Collection (ATCC).

2.2. Preparation of FA-APTES

Twenty mg of FA were dissolved in 2 mL of DMSO followed by addition of 6 mg of NHS and 10 mg of EDC and stirring for 30 min. Subsequently, 50 μL of APTES were added, and the mixture was allowed to react for 48 hours under nitrogen.

2.3. Preparation and functionalization of NPAPF@SiO_2-FA NPs

NPAPF and poly(maleicanhydride-alt-1-octadecene)-poly(ethyleneglycol) (C18PMH-PEG) were synthesized as stated in literature [20,23]. Solvent exchange method was used to prepare NPAPF NPs. Briefly, 100 μL of 1 mM NPAPF/THF solution were added dropwisely into 5 mL of aqueous solution. After stirring at 1000 rpm for 5 min, the sample was left to stabilize for 72 h. NPAPF@SiO_2-FA NPs were synthesized according to a previously described classical method [24]. Fifty mg of CTAB were added into 30 ml of prepared NPAPF NPs solution followed by vigorous stirring for 30 min. The oil-in-water microemulsion was heated to 40 ºC and aged at

the temperature for 10 min to evaporate tetrahydrofuran. One hundred μL of 2 M NaOH solution were added, and the mixture was heated to 55 ºC. Then, 100 μL of TMOS and 1 mL of ethylacetate were slowly added to the reaction solution in sequence. After 1 h reaction, 250 μL of APTES-FA were added. Ten min later, 25 μL of APTES were filled and the solution was stirred for 12 h. Subsequently, the as-synthesized NPAPF@SiO_2-FA NPs were washed 3 times with 4 ºC water to remove the unreacted species and then dispersed in water. To extract CTAB from the NPs, 10 μL of HCl were added to the dispersion (pH=1.4) and stirred for 3 h at 60 ºC. Finally, 300 μL of 1mg/mL C18PMH-PEG/H_2O were added to 10 mL of NPAPF@SiO_2-FA NPs solutions to modify the surface of the NPs. After ultrasonic treatment for 5 min, the solutions were stored at 4 ºC.

2.4. Characterization

A number of drops of NPAPF@SiO_2-FA NPs suspensions were placed slowly onto a silicon substrate. After drying, a 2-nm thick gold layer was deposited on the samples for SEM observation with FEI Quanta 200 FEG. The size of the NPs was measured by dynamic light scattering (DLS) at 25 ºC. UV-vis absorption spectra were recorded with a Perkin-Elmer Lambda 750 UV/vis/NIR spectrophotometer. Fluorescence spectra were measured with a Horiba JobinYvon luminescence spectrometer FluoroMax 4.

The fluorescence quantum yield of the NPAPF@SiO_2-FA NPs in aqueous solution was measured using 2,7-di(4-(diphenylamino)phenyl-2,1,3-benzothiadiazol-7-yl) -9,9'-spirobifluorene (Spiro-BTA) (QY = 0.45) as a standard. The quantum yield was

calculated according to the following equation:

$\eta_s=\eta_r * (A_r/A_s) * (I_s/I_r) * (n_s^2/n_r^2)$

Where η_r and η_s are the fluorescence quantum yield of reference material (standard) and sample, respectively; A_r and A_s the absorbance of reference and sample at a certain excitation wavelength, respectively; I_r and I_s the total emission intensity of reference and sample at an excitation wavelength, respectively; n_r and n_s the refractive index of the solvent of reference and sample, respectively. The absorbance value A was remained below 0.05 during the measurement. The refractive index of water and THF at 20 ºC is 1.33 and 1.4, respectively.

The release kinetics of the dye molecules from NPAPF@SiO_2-FA NPs was investigated with the following procedures. Firstly, 30 μM of NPAPF@SiO_2-FA NPs were dispersed in 1.5 mL of water. Secondly, the samples were centrifuged to precipitate the NPs at different time points. Thirdly, the fluorescence intensities of the supernatant and the precipitated NPs were all measured.

2.5. Cell culture

KB cells were cultured in FA free RPMI-1640 medium containing 10% FBS and 1% penicillin/streptomycin solution. HL-7702 cells were cultured in normal RPMI-1640 medium with 10% FBS and 1% penicillin/streptomycin solution. The concentrations of FA in FA-free and normal culture medium were 3 nM and 2.26 μM, respectively. All cells were cultured at 37 ºC in a humidified atmosphere containing 5% CO_2.

2.6. In vitro cytotoxicity

HL-7702 cells in complete RPMI-1640 medium，or KB cells in FA free RPMI-1640

medium were placed in 96-well plates (50,000/well) followed by 24 h incubation. The media were then replaced with fresh ones containing different concentrations of NPAPF@SiO_2-FA NPs. The cell incubation was maintained for 24, 48 or 72 h in different groups. Then the cells were treated with 20 µL of MTT solution (5 mg/mL in PBS) and the plates were incubated for another 5 h at 37 ºC. After that the medium in each well was removed and 150 µL of DMSO was added to dissolve the formed formazan crystals. Finally, the cell viabilities were determined by measurement of the absorbance.

2.7. FA targeted NPAPF@SiO_2-FA NPs for in vitro imaging

KB cells were cultured in 24-well plates (800 µL of FA-free medium in each well), 200 µL of 15 µM NPAPF@SiO_2 NPs and NPAPF@SiO_2-FA NPs were added separately into different groups followed by incubation at 37 ºC for 4 h. In the two control groups, KB cells were pre-incubated at 4 ºC for 1 h and then each group was incubated with either NPAPF@SiO_2 NPs or NPAPF@SiO_2-FA NPs at 4 ºC for 4 h. The cells were then labeled with blue-colored nuclei-specific DAPI. Confocal microscopy observation of the cells was performed on a Leica laser scanning confocal microscope. For DAPI channel, the excitation was set as 405 nm and the emission was collected in the range of 420–480 nm. For NPs, the excitation was 488 nm and the emission was 580–700 nm. All cells were washed twice with cell culture medium before imaging. The fluorescence intensities were further measured by flow cytometry for quantitative analysis.

2.8. Photo-stability test of NPAPF@SiO_2-FA NPs in living cells

KB cells maintained with FA-free RPMI-1640 medium were plated onto 35 mm glass-bottom cell culture plates. KB cells subcultured from the same source were stained either with 3 μM NPAPF@SiO_2-FA NPs or FITC with same concentration for 4 h. Before imaging, the cells were washed for three times. All groups of cells were excited by 20% power of argon laser (λ_{ex} = 488 nm). The irradiation time interval was 1.315 s. The collected emission windows of NPAPF@SiO_2-FA NPs and FITC are in the ranges of 580-700 and 505-600 nm, respectively. The fluorescence intensities of the samples were normalized in relative to the initial intensity of the first scan of NPAPF@SiO_2-FA NPs and FITC stained cells.

2.9. Cellular uptake of NPAPF@SiO_2-FA NPs

KB cells were seeded in 35 mm diameter glass dishes with a cell density of 1×10^5 cells/mL. After reaching 60% confluence, the cells were treated with 3 μM NPAPF@SiO_2-FA NPs for 4 h. At different time points, cells were observed with a confocal laser scanning microscope equipped with CO_2 and temperature control through imaging. Cell division studies were carried out during the cellular uptake progress. The concentration of NPAPF@SiO_2-FA NPs was 6 μM.

2.10. Cellular uptake pathways

The effect of temperature on the cellular uptake was investigated by pre-incubating KB cells in a serum-free medium at 4 ºC for 1 h and then incubated with NPAPF@SiO_2-FA NPs at the same temperature for 4 h. In different groups, KB cells were pre-incubated with various inhibitors including chlorpromazine (10 μg/mL) to inhibit the formation of clathrin vesicles, cytisine (1 μg/mL) to inhibit caveolae, and

amiloride (50 μM) to inhibit micropinocytosis. The incubation was all at 37 ºC and for 1 h. Subsequently, the inhibitor solutions were removed, NPAPF@SiO_2-FA NPs in media containing inhibitors with the same concentrations were added and further incubated at 37 ºC for 4 h. As a control group, cells were incubated with NPAPF@SiO_2-FA NPs without inhibitor treatment. The cells were washed with ice cold PBS for three times, and fixed with fresh 4% paraformaldehyde for 5 min at room temperature. The nuclei of the cells were stained with DAPI and visualized under confocal laser scanning microscopy (CLSM). The fluorescence intensities were measured by flow cytometry for quantitative analysis.

2.11. Colocalization of NPs and lysosomes

KB cells were incubated with 50 nM LysoTracker Green DND-26 at 37 ºC for 30 min and then with NPAPF@SiO_2-FA NPs (3 μM) for an additional 4 h. After incubation, the cells were washed with ice cold PBS and fixed for visualization.

2.12. Active transport of internalized NPAPF@SiO_2-FA NPs

Three μM of NPAPF@SiO_2-FA NPs were added into KB cells and incubated for 4 h at 37 ºC to allow particle internalization. Then the medium was removed. Cells were then washed several times with PBS in order to remove NPAPF@SiO_2-FA NPs that were not internalized. Finally, the motions of endocytosed NPAPF@SiO_2-FA NPs within the cells were recorded by time-lapse acquisition of image every 1.315 s. To study the cellular uptake and intracellular transport inhibition effect of cytoskeleton-disrupting drugs, 5 μM of cytochalasin D and 30 μM of nocodazole were applied to the cells for 30 min to disrupt actin filaments and microtubules,

respectively. Then the cells were further treated with NPAPF@SiO_2-FA NPs for 4 h before confocal microscopy observation.

2.13. Kinetics of exocytosis of NPAPF@SiO_2-FA NPs

For investigating the exocytosis of nanostructures, KB cells were incubated with 3 μM NPAPF@SiO_2-FA NPs for 4 h to get a substantial intracellular uptake. Then, the cells were washed three times with PBS and placed in a fresh cell culture medium. At different time points, an aliquot of the medium was collected and its fluorescence intensity was determined.

2.14. In vivo NIR fluorescence imaging

All in vivo experiments were performed in compliance with the relevant laws and institutional guidelines and also approved by Laboratory Animal Center of Soochow University. The BALB/c female mice with age of 5 to 6 weeks were purchased from Suzhou Industrial Park Animal Technology Co., Ltd. and were housed in a standard facility. 4T1 tumor-bearing mice were intravenously injected with 200 μL of 60 μM NPAPF@SiO_2-FA NPs and imaged using a Maestro in vivo fluorescence imaging system (CRi Inc.). Green light with a peak wavelength at 523 nm was used as the excitation source. Spectral imaging from 600 nm to 750 nm (10 nm step) was carried out with various exposure times for each image frame. Autofluorescence (particularly from food residues in the stomach and intestine) was decreased by exposure time. The mouse was marked out by green line in situ corresponding with the bright-filed image.

2.15. Biodistribution

4T1 bearing BALB/c mice were just treated with NPAPF@SiO_2-FA NPs at a dose

of 200 μL and then were sacrificed at 1, 2, 6, 12, 24 and 48 h. Fluorescence of various organs and tissues were spectrally measured by the Maestro system. The averaged fluorescent intensity was calculated for a semi-quantitative biodistribution analysis.

3. Results and discussion

3.1. Synthesis and characterization of NPAPF@SiO_2-FA NPs

NPAPF is an AIE dye with weak fluorescence in THF. We firstly used a solvent exchange method to prepare NPAPF NPs in aqueous solution. Subsequently, a very thin silica layer was grown on NPAPF NPs (termed NPAPF@SiO_2) followed by anchoring FA molecules on the surface to produce NPAPF@SiO_2-FA NPs. Growth of an optically transparent SiO_2 layer is to improve the stability of the NPs. Attachment of FA on the surface of the NPs is for targeted delivery to specific cells with folate receptors (FR) [25]. SEM and TEM images of NPAPF@SiO_2-FA NPs are displayed in Fig. 1a and 1b. These NPs are spherical in shape and have an average diameter of 90 nm. DLS analysis shows their average hydrodynamic diameter is approximately 120 nm (Fig. S1b). There is a thin silica shell of about 10 nm coated on the surface of the NPs (Fig. S2a), and this can be confirmed by the EDX analysis presented in Fig. S2b. The successful linkage of FA to the surface of NPAPF@SiO_2 NPs is demonstrated by the FTIR spectrum (Fig. S4).

The optical properties of NPAPF in THF and NPAPF NPs in aqueous solution are shown in Fig. 1c. The emission of the THF solution of NPAPF is extremely low. However, after making it into NPs in aqueous solution, the material is strongly

luminescent with a peak at 650 nm. The fluorescence intensity of NPAPF@SiO_2-FA NPs is higher than that of the NPAPF NPs with the same concentration. It is possibly due to the protection of the inert silica shell. Attractively, the NPs display a large Stokes shift of ~175 nm and intense emission in NIR region. Beyond the excellent optical properties of the NPs, C18PMH-PEG can be used to modify the material and this enables the nanostructures to be water-dispersible, bio-compatible and highly stable [26-28]. After surface functionalization, the size of the NPs shows a slight increase (Fig. S1b). The modified NPs can largely maintain their size and fluorescence in different media spanning from water, PBS, and serum to solutions of various pH values (2-10) during the 80 h observation period (Fig. 1d and Fig. S5a). In aqueous solution, the fluorescence intensity of the NPAPF@SiO_2-FA NPs is stable. During 48 hours period of time, only about 4% of the dye molecules is released (Fig. S3). The QY of NPAPF@SiO_2-FA NPs was measured to be 11.8%. Overall, all of these features make the NPs particularly suitable for in bioimaging.

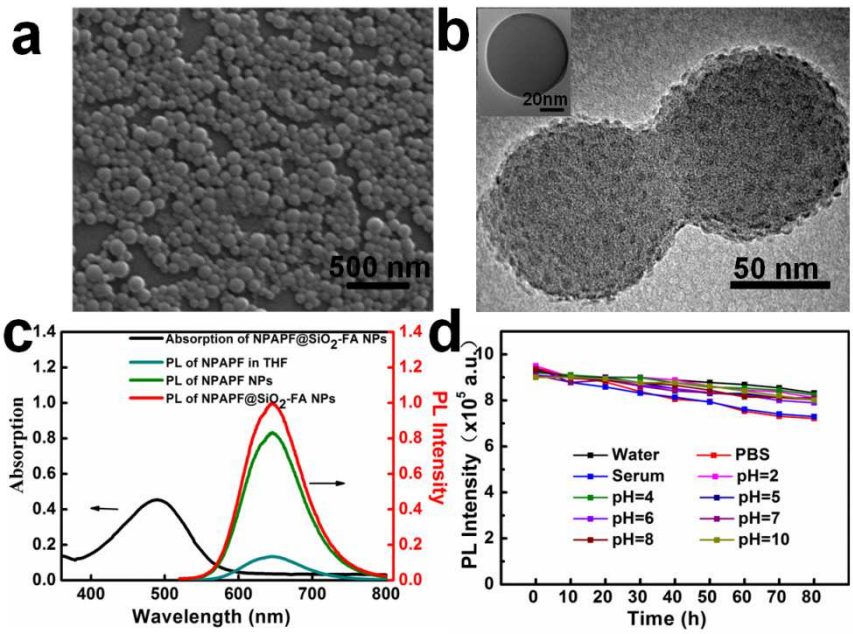

Fig. 1. (a) SEM images of NPAPF@SiO_2-FA NPs; (b) TEM images of NPAPF@SiO_2-FA NPs and NPAPF NPs without a layer of silica coating (inset); (c) UV-vis absorption spectrum of NPAPF@SiO_2-FA NPs and photoluminescence (PL) spectra of NPAPF in THF, uncoated NPAPF NPs and NPAPF@SiO_2-FA NPs; (d) fluorescence stability of modified NPAPF@SiO_2-FA NPs under different conditions.

Except the excellent stability and optical properties of NPs, good biocompatibility is also essential for their application in live cell imaging. Thus, standard MTT assay was used to determine the potential cytotoxicity of NPAPF@SiO_2-FA NPs. We investigated the viability of two different cell lines including KB and HL-7702 cells when incubated with NPAPF@SiO_2-FA NPs. As shown in Fig. S5, both cell lines exhibit very high viability of greater than 90% after 24, 48, and 72 h incubation with NPAPF@SiO_2-FA NPs at different concentrations from 1.25 to 20 μM. These findings demonstrate that the NPAPF@SiO_2-FA NPs are biocompatible and cause low interference on cell proliferation.

3.2. FA targeted cell imaging

FR commonly over-expresses in many types of cancer cells and are broadly used for targeting delivery of therapeutic molecules and biological probes [29]. KB cells cultured in FA-free medium have high FR expression on their surface. FA–targeted NPs display high affinity properties with the receptor [30,31]. This enables them to rapidly bind to the cell surface. The internalization of NPs into cells can be studied through monitoring their fluorescence within cells by confocal microscopy imaging. The results are presented in Fig. S6a. From the figure, it can be found that, in the KB cells incubated with NPAPF@SiO_2-FA NPs at 37 ºC, the intensity of the red

fluorescence is significantly higher than that in the cells incubated with NPAPF@SiO_2 NPs under the same conditions. Even at 4 ºC at which the endocytosis pathway of the NPs is largely suppressed, we still can obtain a similar finding. This is probably due to the fact that FA plays a crucial role for cellular uptake at 4 ºC [32]. The quantity analysis of the NPs internalization under different conditions was further carried out by flow cytometry. As shown in Fig. S6b and S6c, the fluorescence intensity of NPAPF@SiO_2-FA NPs in KB cells is as high as three times of that of NPAPF NPs at 37 ºC and ten times higher than that of NPAPF NPs at 4 ºC. These results clearly demonstrate FA modified NPs are able to efficiently target FR-positive cells. Because of this, high quality cellular imaging can be realized even with very low concentrations of NPs.

3.3. Long-term imaging

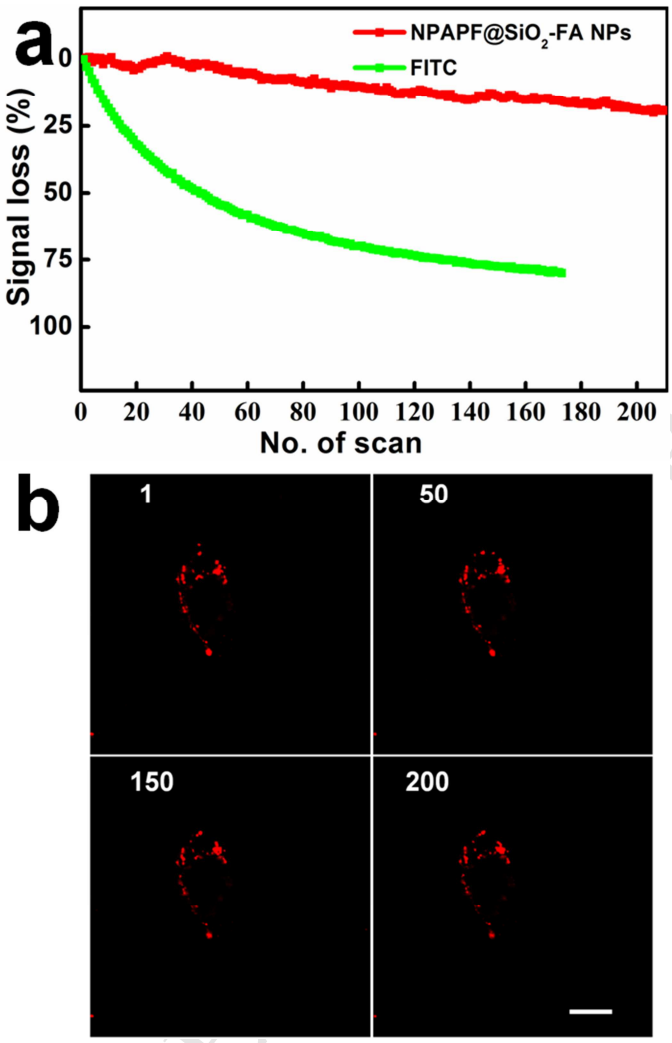

Fig. 2. (a) Signal loss (%) of NPAPF@SiO_2-FA NPs with increasing number of scans. Data for FITC (green curve) are shown for comparison. (b) Fluorescence images of living KB cells incubated with NPAPF@SiO_2-FA NPs at different scans. The numbers of scans are shown in upper left corner. The scale bar indicates 10 μm.

For bioimaging applications, it is highly desirable to allow the fluorescence probe to have a good photo-stability. To study the photo-stability of NPAPF@SiO_2-FA NPs, we carried out an experiment of using the NPs for long-term imaging with an excitation of 488 nm. The imaging of Fluorescein isothiocyanate (FITC) under the same condition was also performed as a reference, as FITC is the most commonly used dye in the field [33,34]. As shown in Fig. 2a, after 211 scans, the signal loss of NPAPF@SiO_2-FA NPs is less than 20% (Movie S1). In a stunning contrast, the

remaining fluorescence signal of FITC is only 20% of the initial value (Movie S2). The direct comparison clearly demonstrates the superior photo-stability of the red-emitting NPAPF@SiO_2-FA NPs, which makes them hold great potential for long-term bioimaging. Fig. 2b shows fluorescent images of KB cells experiencing increasing number of scans when NPAPF@SiO_2-FA NPs were used as a fluorescence probe. It is obvious that the red fluorescence is still ultra-bright after 200 scans.

*3.4. Cellular uptake studi*es

3.4.1. KB cell exposure to NPAPF@SiO_2-FA NPs

Fig. 3 shows the time-dependent fluorescence images of KB cells cultured in FA-free medium at different times after exposure to 3 μM NPAPF@SiO_2-FA NPs. At 30 min after the addition of NPAPF@SiO_2-FA NPs, the outer surface of the cell is visibly stained and the NPs start to gradually accumulate on the surface. Subsequently, more and more NPs are internalized by the cell and transported to the perinuclear region. After 4 h, NPAPF@SiO_2-FA NPs are mostly distributed in the cell peripheries region and perinuclear region. Interestingly, we also observed cell divisions in which the internalized particles are shared by two daughter cells. One example is shown in Fig. 4. This is a clear piece of evidence that the cell division can still occur after cells being treated with NPAPF@SiO_2-FA NPs. Overall, the material has favorable biocompatibility and cells proliferate normally.

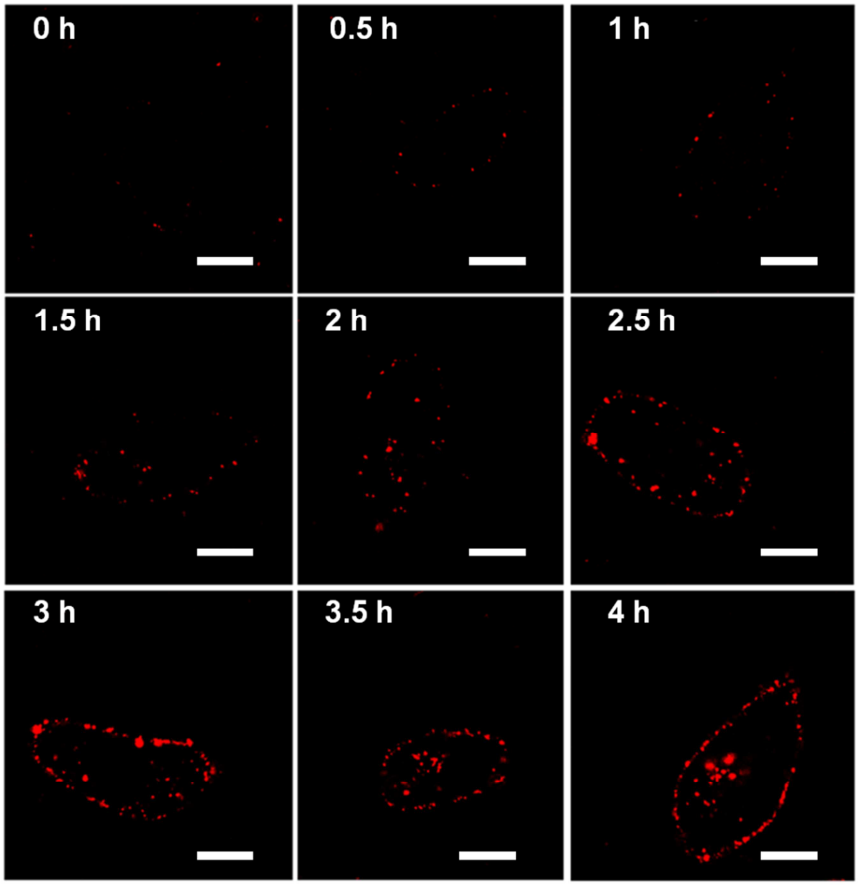

Fig. 3. Time-dependent imaging of NPAPF@SiO_2-FA NPs uptake in cultured KB cells. The experiment was performed under living cell condition (5% CO_2, 37 ºC) with the concentration of NPAPF@SiO_2-FA NPs of 3 μM. Scale bars: 10 μm.

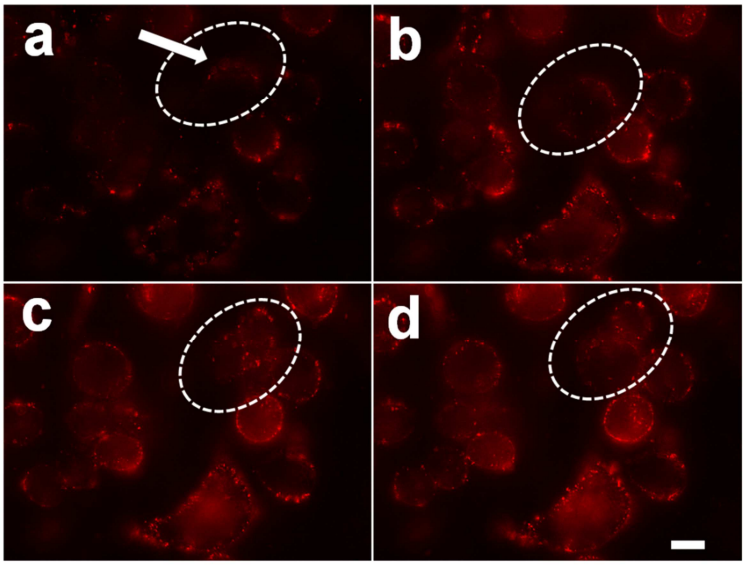

Fig. 4. A KB cell being divided during observation. The internalized NPAPF@SiO_2-FA NPs are shared by the two daughter cells. The concentration of NPAPF@SiO_2-FA NPs was 5 μM. Scale bar: 10 μm.

3.4.2. The endocytic pathways of NPAPF@SiO_2-FA NPs

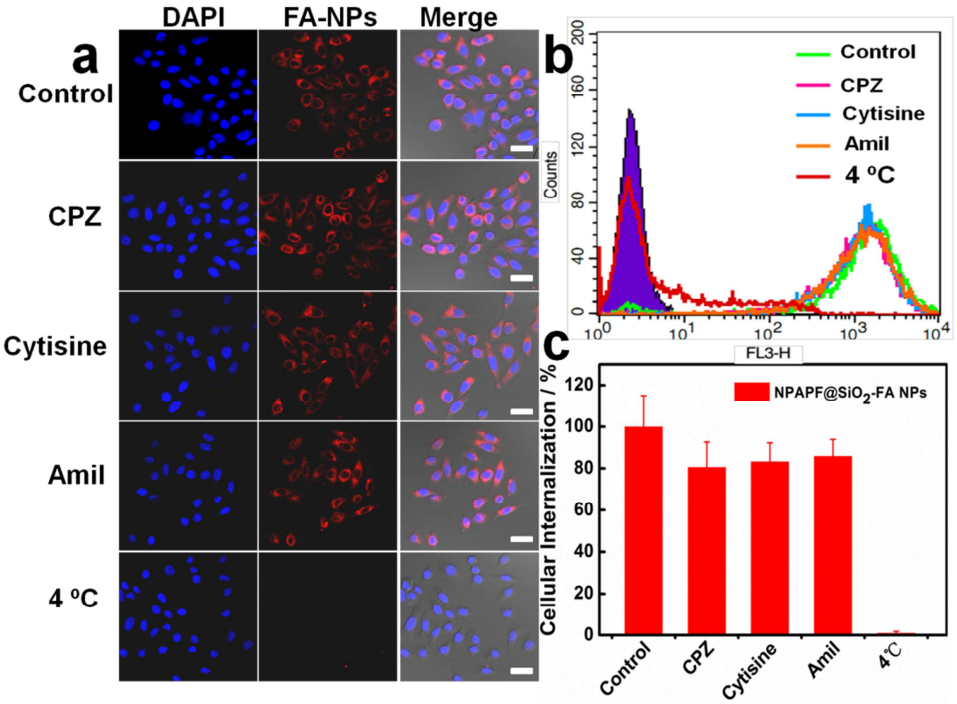

Fig. 5. Effect of different inhibitors on the intracellular uptake of NPAPF@SiO_2-FA NPs. KB cells were either untreated or pre-treated with 10 μg/mL of chlorpromazine, 1 μg/mL of cytisine, or 50 μM of amiloride. Chlorpromazine, cytisine, and amiloride were applied to inhibit clathrin-mediated endocytosis, caveolae and micropinocytosis, respectively. In another group, cells were cultured for 1 h at 4 ºC for energy inhibition. Subsequently, cells were treated with NPAPF@SiO_2-FA NPs for 4 h without washing. The energy inhibition group was still kept at 4 ºC. (a) Confocal microscopy images displaying intracellular uptake of NPAPF@SiO_2-FA NPs (red fluorescence). The cell nuclei were stained by DAPI and are shown in blue. (b) The intracellular uptake of NPs was further quantitatively analyzed by flow cytometry and the corresponding data are illustrated in the graph (c). The scale bars in (a) are 20 μm.

Once we demonstrate that NPAPF@SiO_2-FA NPs can be used for long-term live cell imaging and the cell behavior (e.g., division) is not negatively affected by the treatment of such NPs, we next performed a systematic study to explore the cellular uptake mechanism of the NPs. When cells are pre-incubated at low temperature (4 ºC), the cellular uptake of NPAPF@SiO_2-FA NPs is significantly inhibited (Fig. 5a). It suggests that the endocytosis of NPAPF@SiO_2-FA NPs is an energy-dependent process. Subsequently, three endocytosis inhibitors including chlorpromazine, cytisine,

and amiloride were employed to inhibit clathrin-mediated endocytosis, caveolae-mediated endocytosis, and micropinocytosis, respectively [35]. As shown in Fig. 5a, b, and c, all of the inhibitors retard the cellular uptake of NPAPF@SiO_2-FA NPs to different extents. When KB cells are pre-incubated with CPZ, cytisine and amiloride, the reductions of cellular uptake are 20%, 17% and 14%, respectively, comparing with the control group. However, none of these inhibitors leads to predominant inhibition of intracellular uptake, so it is most possible that clathrin- and caveolae-independent endocytosis plays a crucial role in the internalization of the NPs. After silica coating, the surface topography of NPs changed. Nude NPs have a very smooth surface but the surface becomes relatively rough after the coating which may induce these NPs enter cells via clathrin- and caveolae-independent endocytosis pathway not the normal way. However, the detailed reason of this unique endocytosis pathway for NPAPF@SiO_2-FA NPs still require extensive further work [36,37].

3.4.3. Intracellular fate of NPAPF@SiO_2-FA NPs

Generally, if NPs are internalized by cells through clathrin-mediated endocytosis, the materials will be enclosed into endosomes and lysosomes. Because of the ultra-low pH values and enzymes in these organelles, the enclosed material can be degraded [38]. In comparison, pathways such as caveolar uptake, macropinocytosis and clathrin- and caveolae-independent uptake are somewhat nonspecific and the transport environment is neither acidic nor digestive. To determine the distribution of NPAPF@SiO_2-FA NPs with cells, we stained the lysosomes and applied confocal microscopy imaging for observation. In Fig. S7, lysosomes are stained with green

fluorescence and NPAPF@SiO_2-FA NPs displayed in red. If yellow fluorescence is observed in the merged images, it will suggest that the NPAPF@SiO_2-FA NPs have been located in the lysosomal compartments. However, yellow signal is rarely seen in the overlay. Apparently, almost all NPs are distributed in the cytoplasm and only very few are trapped within lysosomes. Therefore, this pathway is different from the classical endo/lysosomal trafficking form for the intracellular delivery of nanomaterials and may serve as a promising endocytosis pathway avoiding lysosomal degradation of the internalized materials. Non-clathrin and non-caveolae uptake pathway results in non-degradative cellular uptake and prompt perinuclear accumulation. This advantage has already been used for cancer therapy. For example, polymer-based nanoparticle systems deliver drug and gene directly to the perinuclear region which can avoid being degraded in the lysosomers [39], thus delivery efficacy is able to be greatly enhanced. Similarly, fluorescent probes internalized through clathrin- and caveolae-independent pathway can also prevent from being degraded within the enzyme-rich and low-pH environment so that they can maintain strong fluorescence intensity, which is very beneficial for long-term imaging.

3.5. Active transport of internalized NPAPF@SiO_2-FA NPs

After NPAPF@SiO_2-FA NPs are internalized into cells, they are able to transport from one place to another. Real-time images can be employed to visualize the movement of the NPs. In our study, we successfully discovered that some individual NPs originally at the periphery region of cells are transported to the nucleus with an example shown in Fig. 6a. One explanation is that NPAPF@SiO_2-FA NPs are actively

transported by intracellular motor proteins on the microtubules or actin filaments [40].

To confirm this, inhibition studies at the early uptake stage were carried out. We pre-incubated KB cells with cytoskeleton disrupting drugs including 30 μM of nocodazole and 5 μM of cytochalasin D whose roles are to inhibit the polymerization of microtubules and disrupt the actin filaments, respectively [41]. As shown in Fig. 6c, application of the microtubule-disrupting nocodazole leads to a decreased appearance of NPAPF@SiO_2-FA NPs inside the center of the cell and most NPs locate in the cell periphery without moving to the perinuclear area. Employment of cytochalasin D also causes strong suppression of internalization. However some NPAPF@SiO_2-FA NPs can still reach perinuclear region. These results reveal that microtubule-dependent motor proteins like dyneins and kinesins are liable for the transportation of the NPs. Dyneins are responsible for transporting vesicular cargos toward the end of the microtubules near the nucleus, while kinesins possess similar function but moving materials from the nucleus to the cell periphery region [42,43]. For the trajectory observation in Fig. 6a (Movie S3), it is most possible that dyneins are playing important roles. Additionally, we also explored that some NPs are transported away from the perinuclear region (Fig. 6b，Movie S4), probably by kinesins.

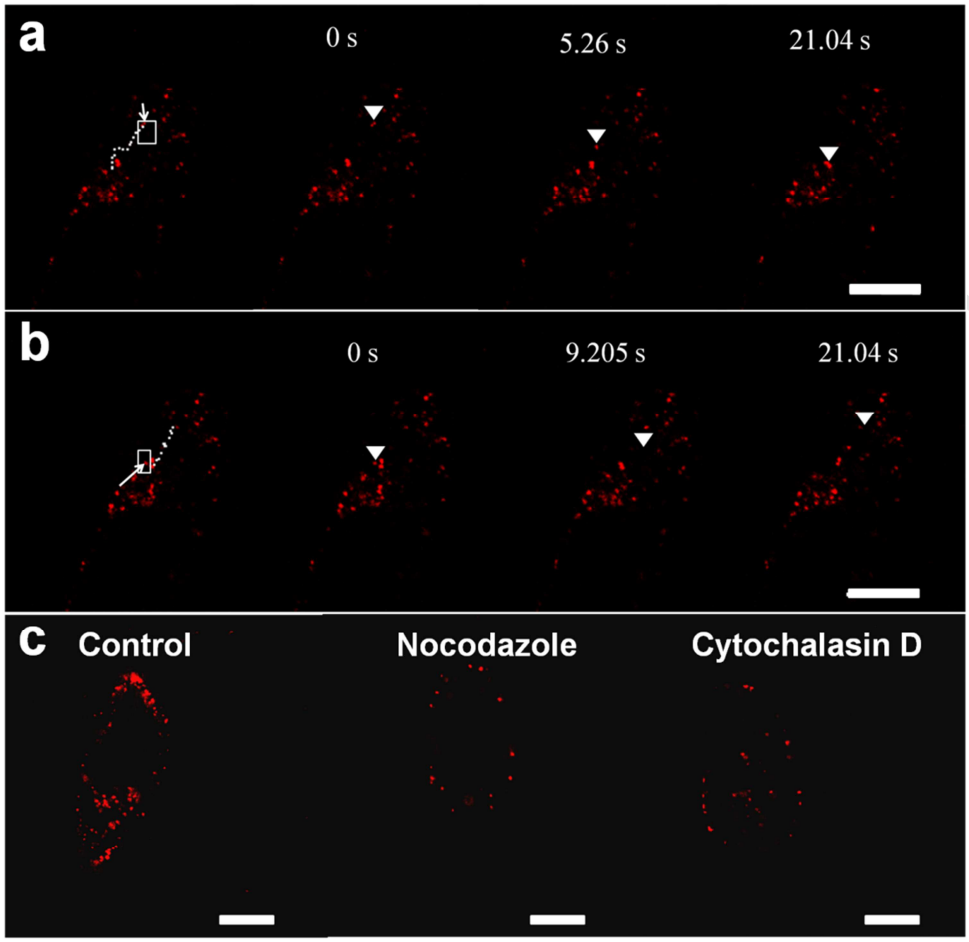

Fig. 6. (a) Trajectory of a nanoparticle transported from the cell periphery to the perinuclear region presumably by dyneins. (b) Trajectory of a nanoparticle transported from the perinuclear region to the cell periphery presumably by kinesins. (c) Inhibition of NPAPF@SiO_2-FA NPs transport by cytoskeleton-disrupting drugs. Confocal images of NPAPF@SiO_2-FA NPs incubated in the absence (control) and presence of the microtubule-disrupting drug nocodazole (30 μM), and actin-disrupting drug cytochalasin D (5 μM). KB cells were treated with the drug for 1h in serum-free media at 37 ºC and were then incubated with 3 μM NPAPF@SiO_2-FA NPs for 4 h. Scale bars: 10 μm.

3.6. NPAPF@SiO_2-FA NPs exocytosed by cells

Exocytosis is one of the behaviors of cells. It has been shown that the retention time of NPs within cells can be influenced by their size, surface properties and endocytic pathways. It has been reported that nanoparticles captured into lysosomes can be exocytosed with lysosomes as the vehicles. While, if nanoparticles have lysosome escape ability, they will stably reside in cytoplasm and the excretion rate will be very

low [37]. In line with this, we can expect NPAPF@SiO_2-FA NPs stay in cytosol and are exocytosed relatively slowly as our mechanism study has shown that they enter cells through non-clathrin and non-caveolae pathway. In order to study the exocytosis of NPAPF@SiO_2-FA NPs, we placed the cells containing internalized nanostructures in a medium and measured the fluorescence intensity of the medium at different times. As illustrated in Fig. S8, the fluorescence intensity increases with extended incubation time and saturates after 8 hours. We speculate that the exocytosis mainly happens to the small fraction of NPs which was internalized through clathrin-mediated endocytosis, while most NPs can still remain in the cytoplasm of cells. Since a large portion of NPAPF@SiO_2-FA NPs can remain within cells for prolonged time, these nanostructures would be desirable for long-term imaging.

3.7. In vivo imaging and biodistribution

NPAPF@SiO_2-FA NPs were examined for in vivo bioimaging applications. NPAPF@SiO_2-FA NPs (200 μL of 60 μM solution for each mouse) were intravenously injected into 4T1 tumor-bearing BALB/c mice. As shown in Fig. S9, at 12 h after injection, the fluorescence of the NPAPF@SiO_2-FA NPs was distinctively bright red and spatially resolved in the tumor site, indicating the preferential accumulation of NPAPF@SiO_2-FA NPs in the tumor. Such a high signal-to-noise ratio is particularly beneficial for NIR probes for cancer diagnosis. We then studied the biodistribution of the NPs by imaging the major organs and the tumor tissues of the 4T1 tumor-bearing BALB/c mouse at different post injection time points (Fig. S10). The fluorescence of NPAPF@SiO_2-FA NPs in the tumor tissues increased with time.

After 48 h post injection, prominent accumulation of NPAPF@SiO_2-FA NPs in tumor sites was observed (56.9% ID g^{-1}). These studies clearly evidenced the advantages of the NPAFN@SiO_2-FA NPs for in vivo imaging.

4. Conclusion

In summary, we fabricated a novel type of FA targeted core-shell organic dye NPs as a fluorescent probe. With the superior characteristics of high fluorescence intensity, large Stokes shift, good photostability, emission in the NIR range, targeted delivery, and biocompatibility, these NPAPF@SiO_2-FA NPs can realize high quality imaging at low concentrations, enabling long-term and real-time imaging in living cells. By using these NPs for imaging, we investigated cell division, the cellular uptake kinetics and pathway of NPs, as well as the distribution and intracellular transport of NPs. Cell division during imaging shows that the cells still remain normal metabolic activities. Cellular uptake of the NPs is time and energy dependent. Clathrin- and caveolae-independent pathway is the main form in the endocytic progress for these unique NPs. The major advantage of as-prepared NPAPF@SiO_2-FA NPs is that these nanostructures enter cells via clathrin- and caveolae-independent endocytosis pathway. This leads to improved intracellular uptake and prolonged stay within cells and correspondingly enhanced fluorescence intensity and potential for long-term imaging/tracking of cells. The capacity of intracellular tracking of specific NPs allows us to use the probe for investigating molecular motors inside living cells. Overall, we prepared an organic fluorescent probe with superior characteristics and successfully

demonstrated its powerful applications in live cell imaging for various studies.

Acknowledgements:

This work was supported by the National Basic Research Program of China (2013CB933500, 2012CB932400), National Natural Science Foundation of China (61422403), Natural Science Foundation of Jiangsu Province (BK20131162), QingLan Project, Collaborative Innovation Center of Suzhou Nano Science and Technology (NANO-CIC), and a Project Funded by the Priority Academic Program Development of Jiangsu Higher Education Institutions (PAPD).

References

[1] D.J. Stephens, V.J. Allan, Light microscopy techniques for live cell imaging, Science 300 (2003) 82-86.

[2] Y.X. Wang, J.Y.J. Shyy, S. Chien, Fluorescence proteins, live-cell imaging, and mechanobiology: seeing is believing, Annu. Rev. Biomed. Eng. 10 (2008) 1-38.

[3] J.K. Jaiswal, E.R. Goldman, H. Mattoussi, S.M. Simon, Use of quantum dots for live cell imaging, Nat. Methods 1 (2004) 73-78.

[4] A. Verma, F. Stellacci, Effect of surface properties on nanoparticle–cell interactions, Small 6 (2010) 12-21.

[5] X.J. Niu, H.Y. Chen, Y.Q. Wang, W.H. Wang, X.Y. Sun, L.X. Chen, Upconversion fluorescence-SERS dual-mode tags for cellular and in vivo imaging, ACS Appl. Mater. Inter. 6 (2014) 5152-5160.

[6] A. Singh, C.K. Lim, Y.D. Lee, J.H. Maeng, S. Lee, J. Koh, et al., Tuning solid-state fluorescence to the near-infrared: a combinatorial approach to discovering molecular nanoprobes for biomedical imaging, ACS Appl. Mater. Inter. 5 (2013) 8881-8888.

[7] Y. Zhou, W.B. Pei, C.Y. Wang, J.X. Zhu, J.S. Wu, Q.Y. Yan, et al., Rhodamine-modified upconversion nanophosphors for ratiometric detection of hypochlorous acid in aqueous solution and living cells, Small 10 (2014) 3560-3567.

[8] K.M. Wang, X.X. He, X.H. Yang, H. Shi, Functionalized silica nanoparticles: a platform for fluorescence imaging at the cell and small animal levels, Accounts

Chem. Res. 46 (2013) 1367-1376.

[9] M.G. Panthani, T.A. Khan, D.K. Reid, D.J. Hellebusch, M.R. Rasch, J.A. Maynard, et al., In vivo whole animal fluorescence imaging of a microparticle-based oral vaccine containing ($CuInSe_xS_{2-x}$)/ZnS core/shell quantum dots, Nano Lett. 13 (2013) 4294-4298.

[10] Y.M. Lu, Y.Y. Su, Y.F. Zhou, J. Wang, F. Peng, Y. L. Zhong, et al., In vivo behavior of near infrared-emitting quantum dots, Biomaterials 34 (2013) 4302-4308.

[11] Y. Zhu, H. Hong, Z.P. Xu, Z. Li, W. Cai, Quantum dot-based nanoprobes for in vivo targeted imaging, Curr. Mol. Med. 13 (2013) 1549-1567.

[12] F.J. Ai, Q. Ju, X.M. Zhang, X. Chen, F. Wang, G.Y. Zhu, A core-shell-shell nanoplatform upconverting near-infrared light at 808 nm for luminescence imaging and photodynamic therapy of cancer, Sci. Rep. 5 (2015) 10785.

[13] S.H. Nam, Y.M. Bae, Y.I. Park, J.H. Kim, H.M. Kim, J.S. Choi, et al., Long-term real-time tracking of lanthanide ion doped upconverting nanoparticles in living cells, Angew. Chem. Int. Edit. 50 (2011) 6093-6097.

[14] N. Chen, Y. He, Y.Y. Su, X.M. Li, Q. Huang, H.F. Wang, et al.,The cytotoxicity of cadmium-based quantum dots, Biomaterials 33 (2012) 1238-1244.

[15] A.M. Derfus, W.C.W. Chan, S.N. Bhatia, Probing the cytotoxicity of semiconductor quantum dots, Nano Lett. 4 (2004) 11-18.

[16] R. Alford, H.M. Simpson, J Duberman, G.C. Hill, M. Ogawa, C. Regino, et al., Toxicity of organic fluorophores used in molecular imaging: literature review,

Mol. Imaging 8 (2009) 341-354.

[17] M.H. Lan, J.F. Zhang, X.Y. Zhu, P.F. Wang, X.F. Chen, C.S. Lee, et al., Highly stable organic fluorescent nanorods for living-cell imaging, Nano Res. 8 (2015) 2380-2389.

[18] P. Sharma, S. Brown, G. Walter, S. Santra, B. Moudgil, Nanoparticles for bioimaging, Adv. Colloid. Interfac. 123-126 (2006) 471-485.

[19] D. Ding, K. Li, B. Liu, B.Z. Tang, Bioprobes based on AIE fluorogens, Accounts Che. Res. 46 (2013) 2441-2453.

[20] Y.L. Yang, F.F. An, Z. Liu, X.J. Zhang, M.J. Zhou, W. Li, et al., Ultrabright and ultrastable near-infrared dye nanoparticles for in vitro and in vivo bioimaging, Biomaterials 33 (2012) 7803-7809.

[21] A.E. Nel, L. Madler, D. Velegol, T. Xia, E.M.V. Hoek, P. Somasundaran, et al., Understanding biophysicochemical interactions at the nano-bio interface, Nat. Mater. 8 (2009) 543-557.

[22] Q.X. Mu, G.B. Jiang, L.X. Chen, H.Y. Zhou, D. Fourches, A. Tropsha, et al., Chemical basis of interactions between engineered nanoparticles and biological systems, Chem. Rev. 114 (2014) 7740-7781.

[23] C. Wang, L. Cheng, Z. Liu, Drug delivery with upconversion nanoparticles for multi-functional targeted cancer cell imaging and therapy, Biomaterials 32 (2011) 1110-1120.

[24] F. Wang, X.L. Chen, Z.X. Zhao, S.H. Tang, X.Q. Huang, C.H. Lin, et al., Synthesis of magnetic, fluorescent and mesoporous core-shell-structured

nanoparticles for imaging, targeting and photodynamic therapy, J. Mater. Chem. 21 (2011) 11244-11252.

[25] K.Y. Pu, B. Liu, Fluorescent conjugated polyelectrolytes for bioimaging, Adv. Funct. Mater. 21 (2011) 3408-3423.

[26] M.J. Zhou, X.J. Zhang, Y.L. Yang, Z. Liu, B.S. Tian, J.S. Jie, et al., Carrier-free functionalized multidrug nanorods for synergistic cancer therapy, Biomaterials 34 (2013) 8960-8967.

[27] H.L. Zuo, Z. Gu, H. Cooper, Z.P. Xu, Crosslinking to enhance colloidal stability and redispersity of layered double hydroxide nanoparticles, J. Colloid. Interf. Sci. 459 (2015) 10-16.

[28] Z. Gu, H. L. Zuo, L. Li, A.H. Wu, Z.P. Xu, Pre-coating layered double hydroxide nanoparticles with albumin to improve colloidal stability and cellular uptake, J. Mater. Chem. B. 3 (2015) 3331-3339.

[29] S. Wang, P.S. Low, Folate-mediated targeting of antineoplastic drugs, imaging agents, and nucleic acids to cancer cells, J. Control Release 53 (1998) 39-48.

[30] L. Yan, W. Chen, X.Y. Zhu, L.B. Huang, Z.G. Wang, G.Y. Zhu, et al., Folic acid conjugated self-assembled layered double hydroxide nanoparticles for high-efficacy-targeted drug delivery, Chem. Commun. 49 (2013) 10938-10940.

[31] L. Yan, J.F. Zhang, C.S. Lee, X.F. Chen, Micro- and nanotechnologies for intracellular delivery, Small 10 (2014) 4487-4504.

[32] R.J. Lee, P.S. Low, Delivery of liposomes into cultured KB cells via folate receptor-mediated endocytosis, J. Biol. Chem. 269 (1994) 3198-3204.

[33] X.J. Hao, M.J. Zhou, X.J. Zhang, J. Yu, J.S. Jie, C.T. Yu, et al., Highly luminescent and photostable core-shell dye nanoparticles for high efficiency bioimaging, Chem. Commun. 50 (2014) 737-739.

[34] A. Sukhanova, L. Venteo, J. Devy, M. Artemyev, V. Oleinikov, M. Pluot, et al., Highly stable fluorescent nanocrystals as a novel class of labels for immunohistochemical analysis of paraffin-embedded tissue sections, Lab. Invest. 82 (2002) 1259-1261.

[35] U.S. Huth, R. Schubert, R.P. Süss, Investigating the uptake and intracellular fate of pH sensitive liposomes by flow cytometry and spectral bio-imaging, J. Control Release 110 (2006) 490-504.

[36] X.L. Hu, J.M. Hu, J. Tian, Z.S. Ge, G.Y. Zhang, K.F. Luo, et al., Polyprodrug amphiphiles: hierarchical assemblies for shape regulated cellular internalization, trafficking, and drug delivery, J. Am Chem. Soc.135 (2013) 17617-17629.

[37] Z.Q. Chu, S.L. Zhang, B.K. Zhang, C.Y. Zhang, C.Y. Fang, I. Rehor, et al., Unambiguous observation of shape effects on cellular fate of nanoparticles, Sci. Rep. 4 (2014) 4495.

[38] H.Y. Nam, S. M. Kwon, H. Chung, S.Y. Lee, S.H. Kwon, H. Jeon, et al., Cellular uptake mechanism and intracellular fate of hydrophobically modified glycol chitosan nanoparticles, J. Control Release 135 (2009) 259-267.

[39] S.K. Lai, K. Hida, S.T. Man, C. Chen, C. Machamer, T.A. Schroer, et al., Privileged delivery of polymer nanoparticles to the perinuclear region of live cells via a non-clathrin, non-degradative pathway, Biomaterials 28 (2007) 2876-2884.

[40] G. Ruan, A. Agrawal, A.I. Marcus, S. Nie, Imaging and tracking of tat peptide-conjugated quantum dots in living cells: new insights into nanoparticle uptake, intracellular transport, and vesicle shedding, J. Am Chem. Soc. 129 (2007) 14759-14766.

[41] G.W. Zieve, Nocodazole and cytochalasin D induce tetraploidy in mammalian cells, American Journal of Physiology - Cell Physiology, 246 (1984) C154-C156.

[42] K. Radtke, K. Dohner, B. Sodeik, Viral interactions with the cytoskeleton: a hitchhiker's guide to the cell, Cell. Microbiol. 8 (2006) 387-400.

[43] R.A. Walker, M.P. Sheetz, Cytoplasmic microtubule-associated motors, Annu. Rev. Biochem. 62 (1993) 429-451.

Supporting Information For

Real-time imaging and tracking of ultrastable organic dye nanoparticles in living cells

Ruirui Xu[a], Liming Huang[a], Weijia Wei[a], Xianfeng Chen[b,*], Xiaohong Zhang[a], and Xiujuan Zhang[a,*]

[a]*Institute of Functional Nano & Soft Materials (FUNSOM), Jiangsu Key Laboratory for Carbon-Based Functional Materials & Devices, Soochow University, Suzhou Jiangsu 215123, P. R. China.*

[b]*School of Chemistry and Forensic Sciences, Faculty of Life Sciences, University of Bradford, United Kingdom, BD7 1DP*

*Correspondence should be sent to E-mails: xjzhang@suda.edu.cn, xianfeng_chen@hotmail.com

Additional data:

Movie. S1. shows long-term imaging of NPAPF@SiO_2-FA NPs with an excitation of 488 nm.

Movie. S2. shows long-term imaging of FITC with an excitation of 488 nm.

Movie. S3. shows the trajectory of a nanoparticle transported from the cell periphery to the perinuclear region.

Movie. S4. shows the trajectory of a nanoparticle transported from the perinuclear region to the cell periphery.

Fig. S1. shows the SEM image of NPAPF NPs without a layer of silica coating and the hydrodynamic diameters of NPAPF NPs, NPAPF@SiO_2-FA NPs and PEGlyated NPAPF@SiO_2-FA NPs.

Fig. S2. shows high-resolution TEM image of NPAPF@SiO_2-FA NPs and the EDX pattern of NPAPF@SiO_2-FA NPs acquired by TEM.

Fig. S3. shows the evolution of the fluorescence intensity of NPAPF@SiO_2-FA NPs and the release kinetics of dye molecules from NPAPF@SiO_2-FA NPs.

Fig. S4. shows the FTIR spectra of FA and FA-APTES.

Fig. S5 shows the size stability of modified NPAPF@SiO_2-FA NPs and cell viabilities.

Fig. S6. shows FA targeted cell imaging.

Fig. S7. shows the distribution of NPAPF@SiO_2-FA NPs and lysosomes within KB cells.

Fig. S8. shows the evolution of the PL intensities of the cell media after incubating with cells for different time points.

Fig. S9. shows in vivo fluorescence image of a mouse at 12 h after injection of the

NPAPF@SiO_2-FA NPs.

Fig. S10. shows spectrally resolved ex vivo fluorescence images of organs.

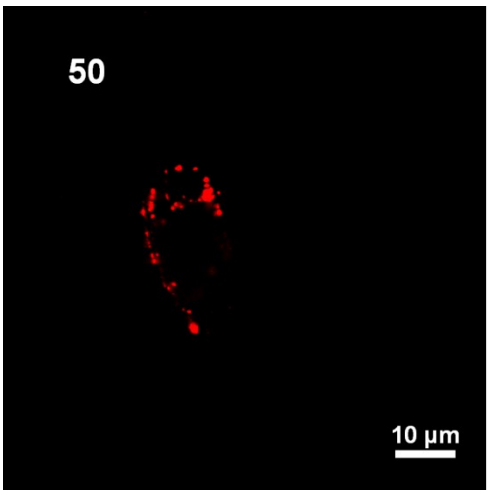

Movie. S1.

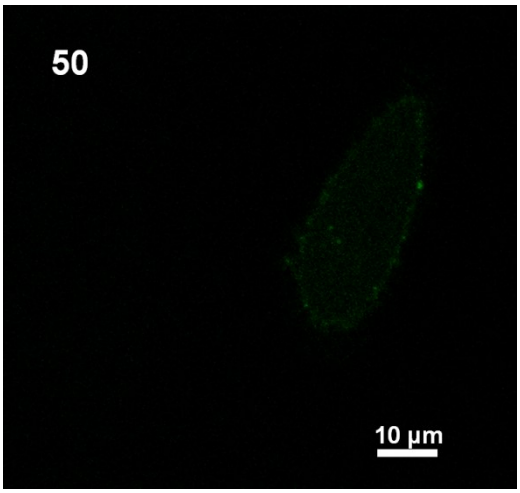

Movie. S2.

Movie. S1-2. Long-term imaging of NPAPF@ SiO_2-FA NPs with an excitation of 488 nm. The imaging of Fluorescein isothiocyanate (FITC) under the same condition was also performed as a reference.

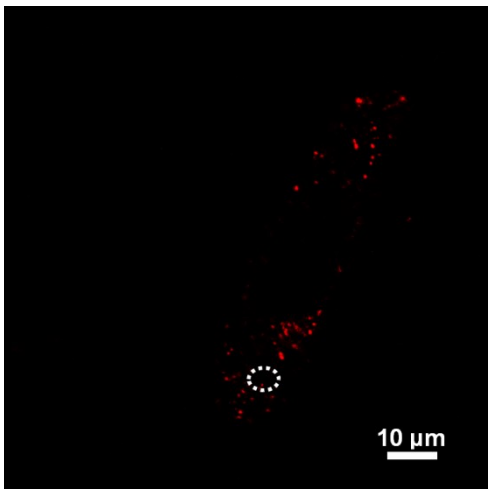

Movie. S3.

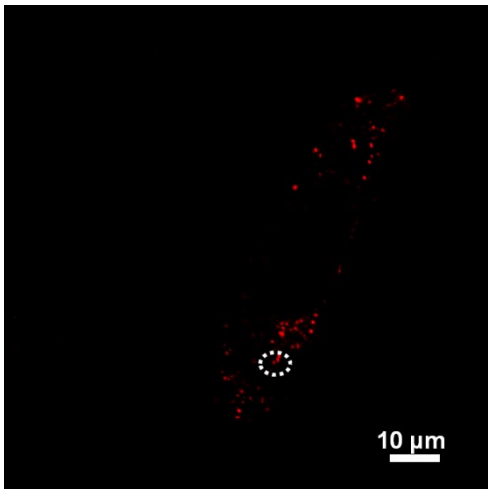

Movie. S4.

Movie. S3. Some NPs are transported from cell periphery to the perinuclear region.

Movie. S4. Some NPs are transported from the perinuclear region to cell periphery.

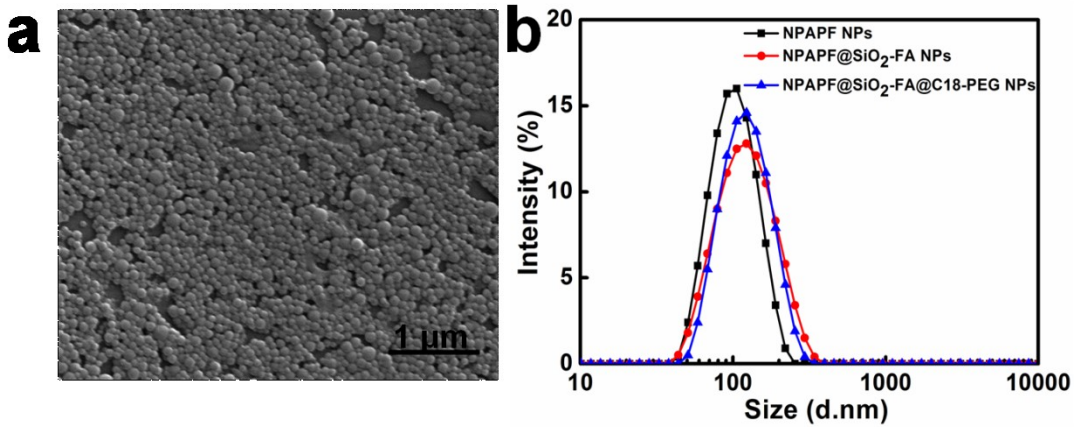

Fig. S1. (a) SEM image of NPAPF NPs without a layer of silica coating (b) The hydrodynamic diameters of NPAPF NPs, NPAPF@SiO_2-FA NPs and PEGlyated NPAPF@SiO_2-FA NPs.

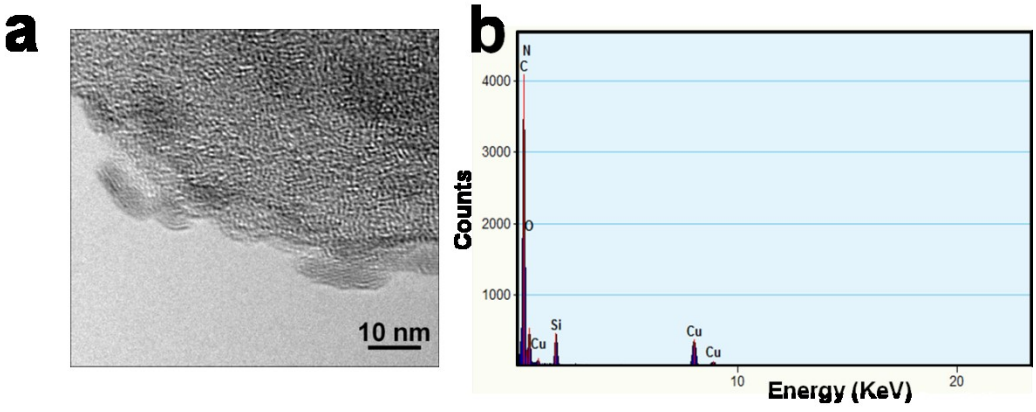

Fig. S2. (a) A high-resolution TEM image of NPAPF@SiO_2-FA NPs. (b) EDX pattern of NPAPF@SiO_2-FA NPs acquired by TEM.

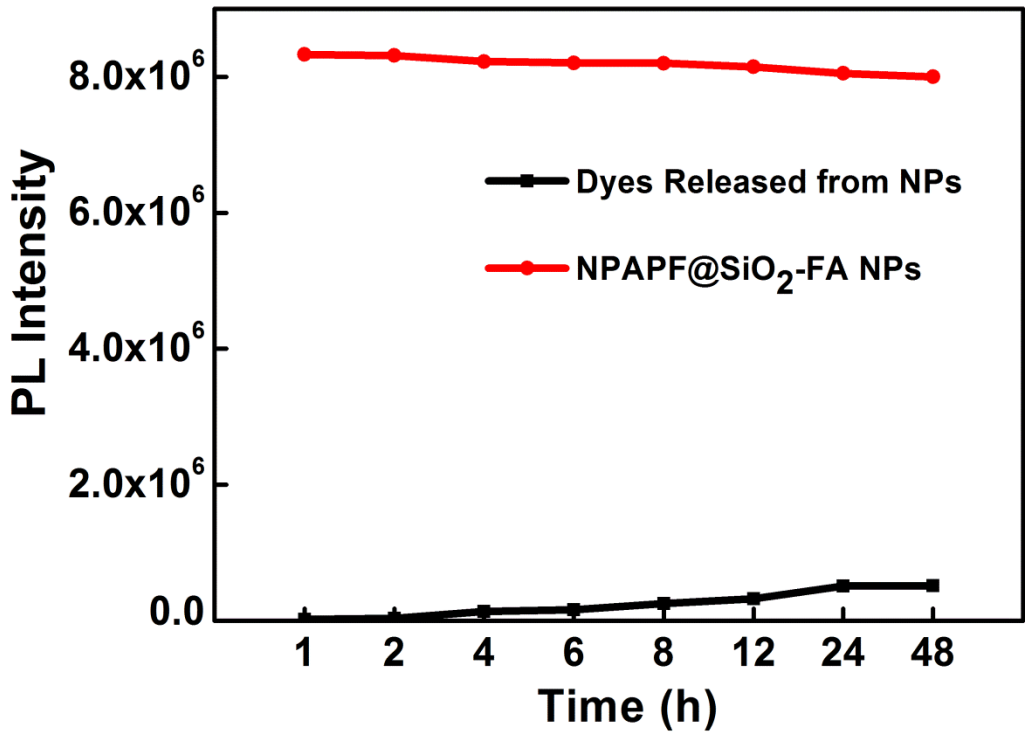

Fig. S3. The evolution of the fluorescence intensity of NPAPF@SiO_2-FA NPs and the release kinetics of dye molecules from NPAPF@SiO_2-FA NPs.

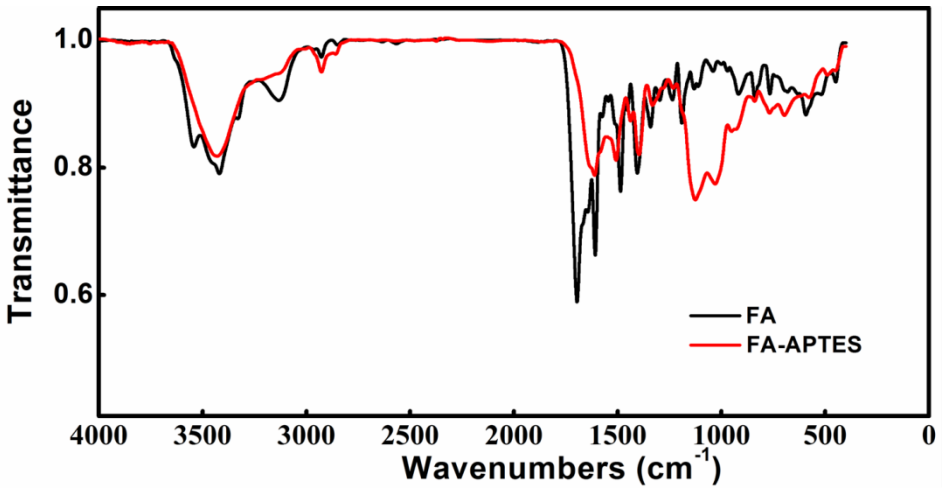

Fig. S4. FTIR spectra of FA and FA-APTES.

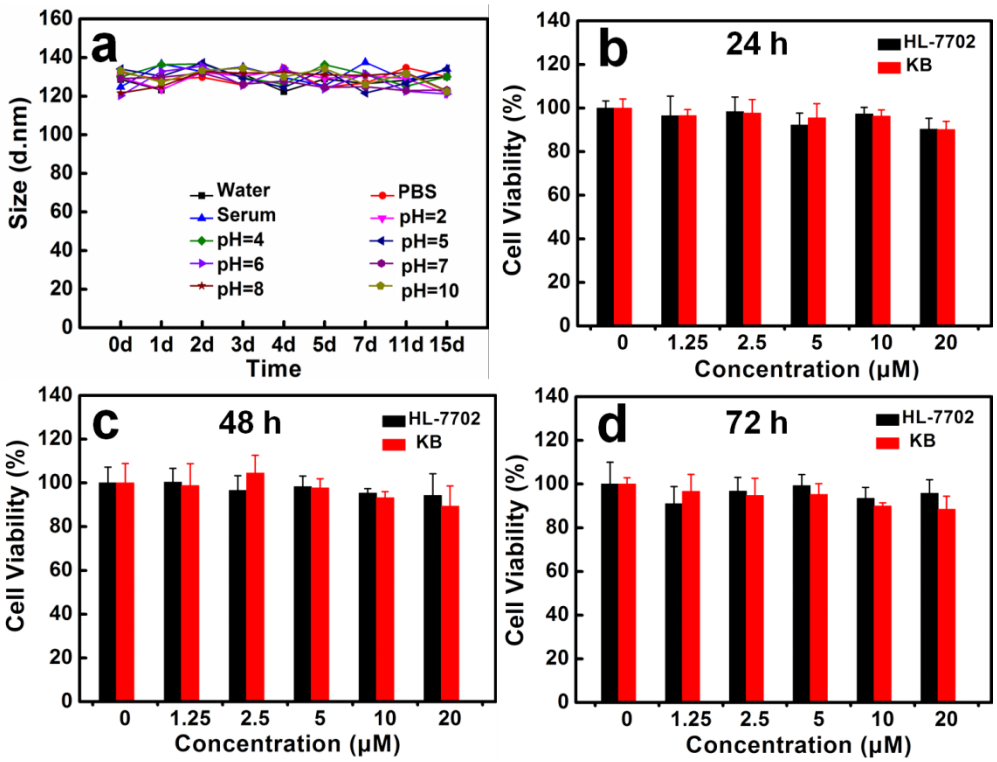

Fig. S5. (a) Size stability of modified NPAPF@SiO_2-FA NPs under different conditions. (b), (c) and (d) present the cell viabilities of KB cells and HL-7702 cells incubated with NPAPF@SiO_2-FA NPs for 24, 48, and 72 h, respectively. The cell viabilities were determined using MTT assay.

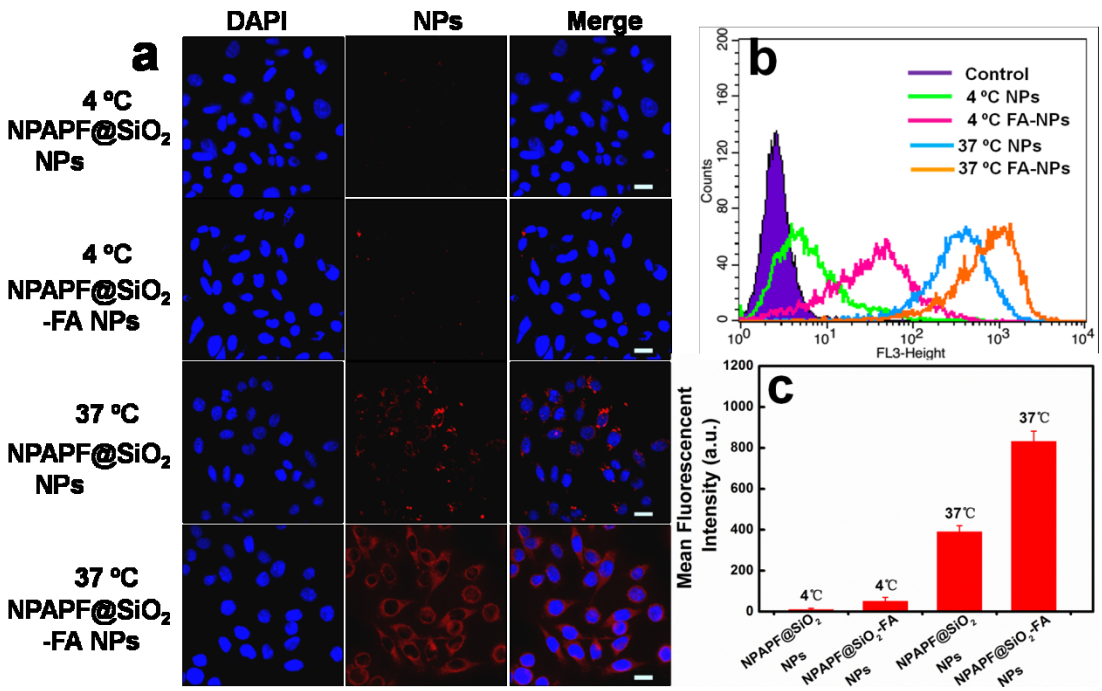

Fig. S6. FA targeted cell imaging. KB cells were cultured in FA-free medium. In two groups, 3 μM NPAPF@SiO_2-FA NPs or NPAPF@SiO_2 NPs were added into cells and incubated at 37 ºC for 4 h. The other two groups of KB cells were pre-incubated at 4 ºC for 1 h and then incubated with either NPAPF@SiO_2 NPs or NPAPF@SiO_2-FA NPs at 4 ºC for 4 h. (a) Confocal images of different NPs uptake at different temperatures. (b) Flow cytometry analysis of cells under various conditions. (c) Quantity analysis of the fluorescence intensities of cells. Values were obtained from the flow cytometry analysis shown in (b). Scale bars: 20 μm.

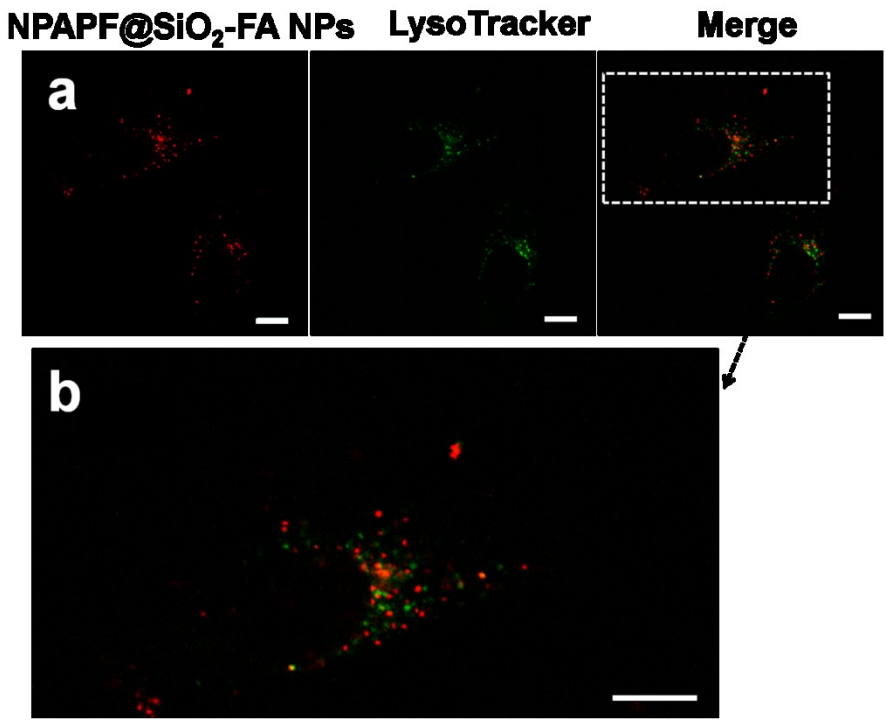

Fig. S7. (a) Distribution of NPAPF@SiO_2-FA NPs and lysosomes within KB cells. Lysosomes were stained with LysoTracker (green). Red fluorescence is from the NPs. Co-localization of NPs with lysosome should appear in yellow in the merged images. Scale bars: 10 μm. (b) Magnified image of the white boxed area in (a). Scale bar: 10 μm.

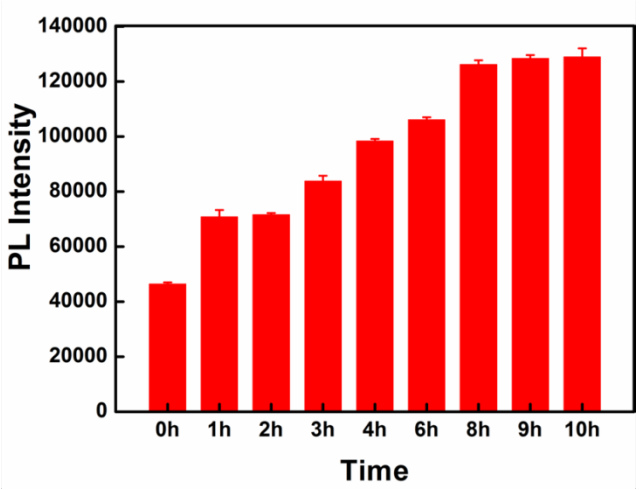

Fig. S8. Evolution of the PL intensities of the cell media after incubating with cells for different time points. NPAPF@SiO_2-FA NPs were internalized into the cells in advance.

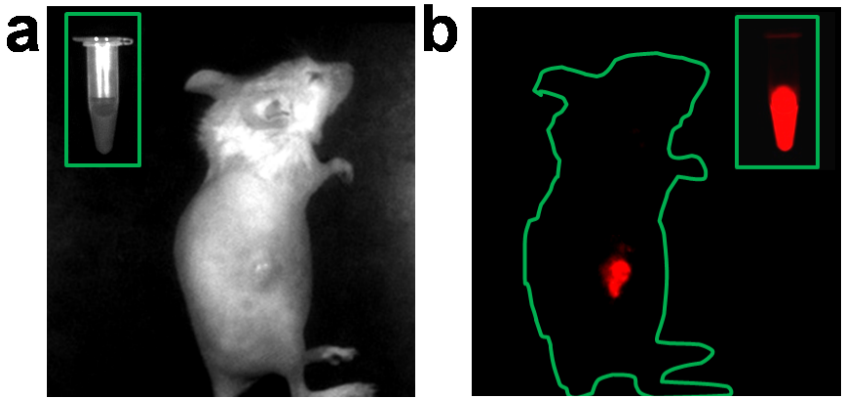

Fig. S9. (a) Bright-field image of a tumor-bearing mouse and NPAPF@SiO_2-FA NPs solution (inset). (b) In vivo fluorescence image of a mouse at 12 h after injection of the NPAPF@SiO_2-FA NPs with 5 ms exposure time. The inset shows the fluorescence image of NPAPF@SiO_2-FA NPs in the storage equipment with 10 ms exposure time.

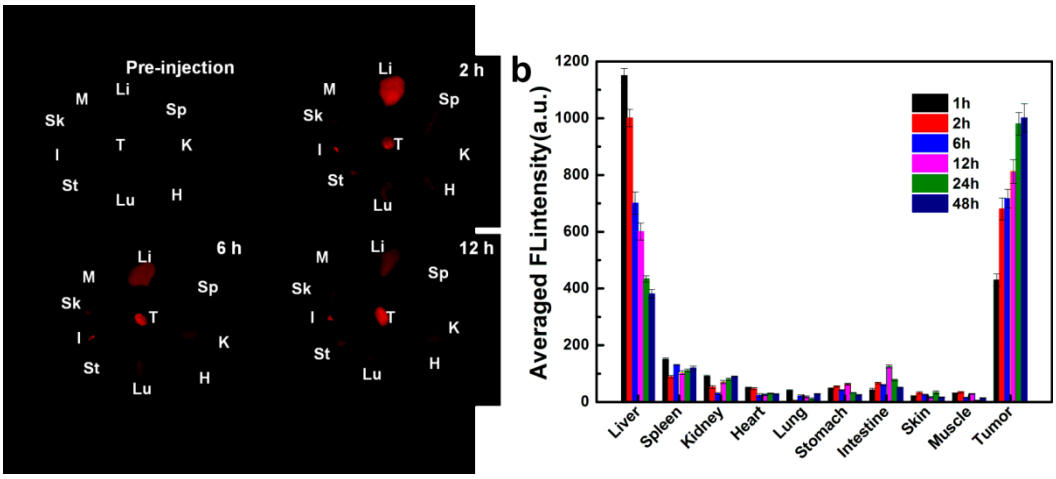

Fig. S10. Spectrally resolved ex vivo fluorescence images of organs before injection and at 2, 6, and 12 h after injection of the NPAPF@SiO_2-FA NPs NPs. Li: liver, M: muscle, Sk: skin, I: intestine, St: stomach, Lu: lung, H: heart, K: kidney, Sp: spleen, and T: tumor. (b) Semi-quantitative biodistribution of NPAPF@SiO_2-FA NPs in mice determined by the averaged fluorescence intensity of each organ (after subtraction of the fluorescence intensity of each organ before injection). Error bars were based on three mice per group.